Vietnam Journal of Science and Technology ***64***(2) (2026) 292–304
DOI: https://doi.org/10.15625/2525-2518/18386

Structural, electrical, and ferroelectric properties of Zn doped $NiTiO_3$

Bui Phi Long[1], Nguyen Tuyet Nga[1], Nguyen Hoang Tuan[1], Pham Van Thang[1], Duong Van Thiet[2], Pham Phi Hung[3], Luong Huu Bac[1,*]

[1]*Faculty of Engineering Physics, Hanoi University of Science and Technology, 1 Dai Co Viet road, Bach Mai ward, Ha Noi, Viet Nam*
[2]*Hanoi University of Industry, 298 Cau Dien road, Tay Tuu ward, Ha Noi, Viet Nam*
[3]*Samsung Display Vietnam Co., Ltd, Yen Phong, Bac Ninh, Viet Nam*

[*]Email: *bac.luonghuu@hust.edu.vn*

Received: 04 September 2023; Accepted for publication: 05 January 2026

Abstract. In this study, the impact of Zn doping on the structural, electrical and ferroelectric properties of $NiTiO_3$ materials prepared by sol-gel method was examined. X-ray diffraction, Raman scattering and scanning electron microscope methods were performed on the fabricated samples to assess their characteristics. Single-phase $Ni_{1-x}Zn_xTiO_3$ (with x = 0, 0.05, and 0.10) materials were successfully obtained. The X-ray diffraction pattern revealed that all the samples were a single phase, that crystallizes in the rhombohedral structure with a $R\bar{3}$ space group. The Zn doped $NiTiO_3$ resulted in an increase in lattice parameter and a decrease in tolerance factor in comparison to the undoped sample. The incorporation of Zn dopant into $NiTiO_3$ leads to a modification of its ionic conductivity. The ac conductivity of all samples followed the Jonscher's power law. The room temperature ferroelectric properties of Zn-doped $NiTiO_3$ ceramics were analyzed. With an increase in Zn concentration, the ferroelectric properties of the Zn-doped samples increased. This can be attributed to the Zn dopant into host $NiTiO_3$ lattice, which created the distortion of lattice. However, heavily dopant concentration can increase the material's conductivity and therefore decreased its ferroelectric parameters. Ferroelectric loops were investigated at room temperature. The hysteresis loops indicated the typical ferroelectric nature of Zn-doped $NiTiO_3$ samples at room temperature.

Keywords: citrate gel method, impedance, dielectric properties, electrical conductivity.

Classification numbers: 2.2.2, 2.9.2, 2.10.3.

1. INTRODUCTION

Nickel titanate, a compound belonging to the ilmenite family with the general formula $MTiO_3$ (M = Ni, Co, Fe, Mn, Zn, Cu), has been recognized as a promising candidate for a wide range of applications. These applications include photocatalysis [1], sonocatalysis [2], electrode for solid oxide fuel cells [3], gas sensors [4], spin electronic devices with magnetoelectric effect [5], paint pigment [6], and anode materials for lithium-ion batteries [7]. Extensive research on $NiTiO_3$ has revealed several notable properties: it exhibits n-type semiconductor behavior with a relatively low bandgap of approximately 2.18 eV, displays antiferromagnetic properties, and

demonstrates low ferroelectric characteristics. The field of $NiTiO_3$-based materials has garnered significant attention, particularly for its potential application in catalysis for the degradation of textile dyes [8-11]. Recent investigations have also highlighted the intriguing magnetic and electric properties of ilmenite $NiTiO_3$ materials. Notably, these materials have shown potential as multiferroics, as evidenced by their antiferromagnetic transition at 14.9 K and a magnetic moment of 4.7 μB [12]. The ferroelectric polarization of $NiTiO_3$ is primarily influenced by Ti ions in the $3d_0$ state, while the antiferromagnetic characteristics are believed to stem from the contributions of Ni ions with partially filled orbitals.

Enhancing the ferroelectric properties of a ferroelectric material involves several factors, including compactness and sintering conditions [13-15], and the type and concentration of doping [16-18]. Research has shown that doping ferroelectric materials with transition metals such as Fe, Co, Mn can alter their optical and ferroelectric characteristics. Various studies have explored doping and compositing approaches to modify the properties of $NiTiO_3$ materials. However, most of these investigations have primarily focused on the structural and optical aspects of $NiTiO_3$ materials.

Pham *et al.* examined the impact of Mo doping on the optical and structural properties of $NiTiO_3$ synthesized using a modified Pechini method [19]. Mo doping improved the optical properties by increasing absorption rates, impeding recombination processes, and resulting in reduced grain size and porosity. Fujioka *et al.* synthesized a solid solution of $Ni_{1-x}Co_xTiO_3$ ($0.05 \leq x \leq 0.80$) through a solid-state technique and studied the structural distortion using Raman analysis [20]. They attributed the observed transition to a mixing of Ni, Co, and Ti cations, leading to a transformation from the ilmenite structure to a disordered structure. The presence of vacant octahedra was suggested to play a significant role in this structural transformation. Al-doped $NiTiO_3$ has been synthesized via a hydrothermal method, exhibiting internal microstrain. Al substitution was reported to influence the optical and electrical responses of $NiTiO_3$, leading to a reduced bandgap and noticeable changes in dielectric behavior as well as grain- and grain boundary-dominated conduction, indicating potential relevance for microwave dielectric applications [21]. Jiang *et al.* investigated the effect of Nb on $NiTiO_3$ photocatalytic properties [22]. They showed that incorporation of Nb into the $NiTiO_3$ lattice induces Ti^{3+} sites and oxygen vacancies. The high number of oxygen vacancies in Nb-doped $NiTiO_3$ photocatalysts induce the low recombination rate of photogenerated electron–hole pairs, which results in high reaction rate constant. Lenin *et al.* reported on ferromagnetic nanoparticles of $Fe^{3+}/NiTiO_3$ [23]. Through impedance analysis, they investigated the ferro-dielectric behavior of $Fe^{3+}/NiTiO_3$ nanoparticles and observed enhanced properties with increasing Fe dopant content. The results indicated that the nucleation reaction rate influenced the improved magnetic nanoparticle properties with higher Fe content. However, no systematic research has been reported thus far on the structural, electrical and ferroelectric characteristics of Zn-doped $NiTiO_3$ at ambient temperature. There have been extensive studies on doping and compositing techniques to modify $NiTiO_3$ materials, focusing mainly on structural and optical properties. While investigations have explored the effects of dopants such as Mo, Co, and Fe, systematic research on the electrical and ferroelectric characteristics of Zn-doped $NiTiO_3$ at high temperature and frequency is still lacking.

In this work, we present the analysis of structural, electrical and ferroelectric properties of Zn doped ilmenite $NiTiO_3$ which was synthesized by a sol gel method.

2. MATERIALS AND METHODS

The Zn-doped $NiTiO_3$ ($Ni_{1-x}Zn_xTiO_3$, x = 0, 0.05 and 0.10) nanoparticles were synthesized using the sol-gel technique. The raw materials used consist of tetraisopropoxytitanium (IV) ($C_{12}H_{28}O_4Ti$), nickel nitrate ($Ni(NO_3)_2.6H_2O$), and iron nitrate ($Zn(NO_3)_2.6H_2O$). The citric acid solution ($C_6H_8O_7$) was selected as the solvent. These chemicals were utilized in the synthesis of the samples used with distilled water. Firstly, two ml of the tetraisopropoxytitanium (IV) was dissolved in citric acid solution at 70 °C. A transparent homogeneous sol was formed after stirring vigorously for 2 hours. Then, the 1.96 g nickel nitrate was introduced with mol of Ni equal to mol of Ti for fabricating of $NiTiO_3$. The additional amounts of zinc nitrate were added to the solution for preparing Zn-doped $NiTiO_3$ samples. The solutions were stirred around 3-4 hours. The solutions were kept stirring around 2 hours and then heated to around 120 °C for a day to prepare dry gels. The dry gels were calcined at 900 °C for 3 hours. The calcined powders were ground in an agate mortar for analysis. XRD measurement was implemented by an X-ray diffractometer (PANalytical X'pert Pro) using Cu Kα radiation. Raman spectroscopy measurements were carried out at room temperature using a micro- Raman spectrometer in combination with a solid state 633 nm laser as the excitation source.

The calcined powder was combined with a small quantity (5 wt.%) of polyvinyl alcohol (PVA) to form a homogeneous mixture. This mixture was subjected to drying at 100 °C for 2 hours. Subsequently, the resulting mixture was compressed into pellets using a cylindrical steel die with a diameter of 10 mm. A uniaxial hydraulic press was employed to apply a pressure of 10^6 N/m^2 to the powder mixtures. The pressed pellets were then heated gradually to 500 °C at a rate of 5 °C/minute, and held at this temperature for 2 hours. Subsequently, the temperature was further increased to 1200 °C with a heating rate of 5 °C/minute, and the pellets were maintained at this temperature for 5 hours under an air atmosphere. The cooling down rate from 1200 °C to room temperature was kept at a heating rate of 5 °C/minute. The micrograph of the sintered pellets was recorded by a scanning electron microscope (SEM). Silver was deposited on both sides of sintered pellets using silver paste for electrical measurement. After deposited, the pellets were dried at 80 °C for 2 hours and then fired at 700 °C for 30 minutes. Impedance spectroscopy of the fabricated Zn doped $NiTiO_3$ samples was carried out using an HP - 4192A impedance analyzer over a frequency range of 1 kHz to 10 MHz and in the wide temperature range. A *P–E* hysteresis loop tracer (Radiant Technologies, Inc.) was used to trace the electrical hysteresis loops.

3. RESULTS AND DISCUSSION

3.1. Structural analysis

The phase purity of synthesized materials was analyzed by the X-ray diffraction method. Figure 1 shows the X-ray diffraction pattern of the $NiTiO_3$ and Zn-doped $NiTiO_3$ samples which were annealed at 900 °C for 3 h. All diffraction peaks observed at 2θ = 24.03°, 32.99°, 35.55°, 40.76°, 49.34°, 53.90°, 57.35°, 62.35°, and 63.97° are matched with the rhombohedral crystal structure (JCPDS 33-0960). No impurity peaks were found in the XRD pattern which confirms that the obtained material is homogeneous and is in a single-phase. These XRD results show that the synthesized powders belong to the rhombohedral crystal structure with R-3 space group. The fact that there is no trace of impurity phases or secondary phases not found from XRD analysis suggests the Zn has successfully substituted for Ni into the lattice of $NiTiO_3$. The peak positions in XRD pattern shift to lower 2θ diffraction angles which is related to the expansion

of the lattice parameter. The lattice parameters were calculated from these XRD data using unit cell software. All position of XRD diffraction peak was carefully fitted using the Gaussian curve by OriginLab pro software. The lattice parameters were evaluated using the UNITCELL-97 program. The lattice parameter as function of Zn dopant was estimated and shown in Table 1. Figure 1(b) shows the magnification of X-ray diffraction patterns of undoped and Zn-doped $NiTiO_3$ samples in 2θ range from 32.5° - 33.7°. The zoom-in XRD peaks show that the peak position of the Zn doped samples slightly shifts toward a higher 2θ value. This result provides evidence that Zn^{2+} cations were incorporated in the lattice structure and replaced on the Ni^{2+} site in lattice. The result exhibits that the lattice parameters of $NiTiO_3$ increase with an increase of Zn dopant concentration. These results happen because of different radius of Ni and Zn ion in lattice. The radius of Ni^{2+} ions is smaller than that of Zn^{2+} ions. According to Shannon's report, Ni^{2+} ions have a radius of 0.69 Å (in the coordination with VI) while Zn^{2+} ions have a radius of 0.74 Å [24]. Therefore, the substitution of Zn cations to the Ni site resulted in the expansion of the lattice parameter.

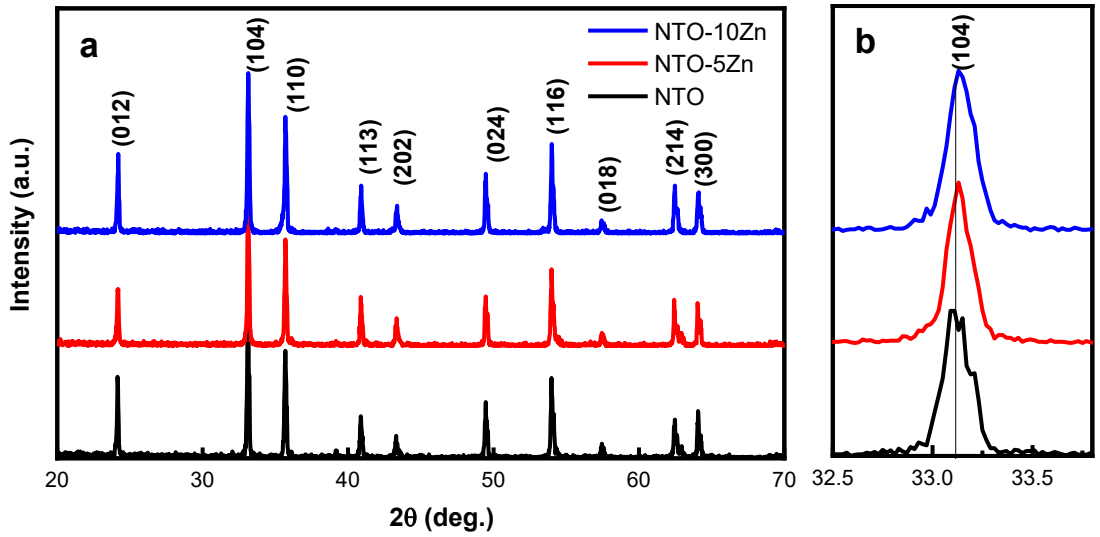

Figure 1. a) X-ray diffraction pattern of Zn-doped $NiTiO_3$ synthesized by the citrate-gel method and b) zoom-in of (104) peak.

The Scherrer crystallite sizes were calculated using all the diffraction peaks appearing in the patterns, according to Scherrer formula $L = k\lambda/\beta\cos\theta$, where λ is the wavelength of the X-ray radiation (Cu K_α = 0.15406 nm), k is the constant related to crystallite shape (k = 0.9), β is the line width at half maximum height, and θ is the diffraction angle. The crystalline grain size calculated by the Scherrer formula is shown in Table 1.. Crystallite size of pure $NiTiO_3$ sample is around 50 nm and slightly increases with Zn doped $NiTiO_3$ sample.

Table 1. Lattice constant and volume of the synthesized Zn doped $NiTiO_3$ samples.

Sample	x	*a* (Å)	*c* (°)	Unit cell volume ($Å^3$)	Crystalline size (nm)	Tolerance factor (t)
NTO	0	5.02735	13.79063	100.62	50	0.9647
NTO-5Zn	0.05	5.03082	13.79750	100.65	55	0.9572
NTO-10Zn	0.10	5.03179	13.80055	100.67	53	0.9499

To analyze the impact of Zn doping on crystal structure stability, we calculated the Goldschmidt tolerance (t) factor, which is defined for an ABO_3-type ilmenite structure as follows [25]:

$$t = \frac{1}{3}\left(\frac{(\sqrt{2}+1)R_{O^{-2}}+R_B}{R_{O^{-2}}+R_A}\right) + \frac{\sqrt{2}\,R_{O^{-2}}}{R_{O^{-2}}+R_B} \quad (1)$$

where R_A, R_B, and R_O are the ionic radii of A, Ti^{4+} (0.605 Å), and O^{2-} (1.4 Å), respectively. Liu *et al.* found in a statistical study of the tolerance factor of various ABO_3-type ilmenites that a tolerance factor of 0.80 or greater is required for a stable ilmenite compound to form [25]. The tolerance factor values of $Ni_{1-x}Zn_xTiO_3$ materials were estimated and are shown in Table 1. As the Zn content increased, the tolerance factor is decreased from 0.9647 for $NiTiO_3$ to 0.9499 for 10 mol.% Zn doped $NiTiO_3$ ceramic. This decline indicates that substituting Zn^{2+} for Ni^{2+} in the $NiTiO_3$ lattice destabilized the ilmenite structure.

3.2. Vibration analysis

Figure 2 shows the Raman scattering of $NiTiO_3$ and Zn-doped $NiTiO_3$ samples at room temperature. The theoretical calculation predicted that the optical normal modes of vibrations of $NiTiO_3$ material have ten active Raman modes 5Ag+ 5Eg [26]. In Figure 2, the ten Raman active modes can be clearly seen which confirm the ilmenite structure of synthesized $NiTiO_3$ materials. The peak positions were estimated to be consistent with recent calculations for vibration modes activity of $NiTiO_3$ materials [27]. The band located at 720 cm^{-1} is related to the Ti-O-Ti vibration of the crystal structure [27]. The band modes at 617 cm^{-1} and 690 cm^{-1} are related to the stretching of Ti-O and bending of O-Ti-O bonds while the vibration mode at 547 cm^{-1} is originated from Ni-O bonds [28]. The vibration modes at 631.9 and 760.5 cm^{-1} result from stretching vibrations of TiO_6 and octahedral vibrations in the region 500-830 cm^{-1} [29]. In addition, the vibration mode at 227.6 cm^{-1} can result from the asymmetric breathing vibration of the oxygen octahedral. Two vibration modes at 290.2 and 434.3 cm^{-1} can be related to the twist of oxygen octahedral because of vibrations of the Ni and Ti atoms parallel to the xy plane [27].

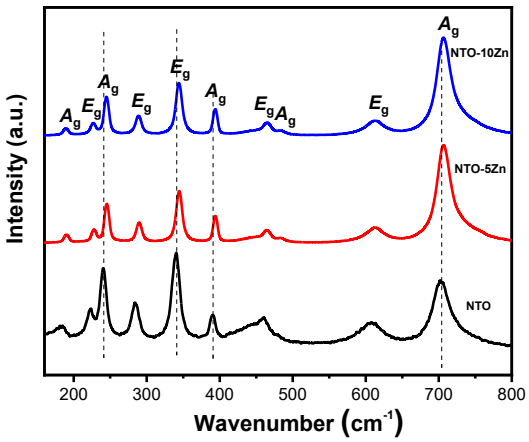

Figure 2. Raman spectra of the Zn-doped $NiTiO_3$ samples.

The Raman analysis shows that ten Raman active modes are observed which confirm the successful synthesis of Zn-doped $NiTiO_3$ materials with ilmenite rhombohedral structure. The shifted peaks in frequency modes to higher frequencies are suggested for distortion $NiTiO_3$ lattice due to Zn cations substitution for Ni in host lattice. Thus, the XRD and Raman scattering

analysis indicate that Zn dopant was well distributed and substituted for Ni in the $NiTiO_3$ host crystal.

3.3. Morphology

Figures 3(a)-(c) show the influence of Zn dopant on the morphology and particle size of the sintered samples. The SEM images show that the surface of the sample had a non-uniform size distribution, and the grain of all the samples was almost irregular and of polygonal structures with clear boundaries. The morphology of the grains appeared smooth and well-arranged. The SEM images reveal a wide distribution in grain size. The overall morphology of the powders was affected by the Zn dopant. When adding Zn as a dopant, the particle size tends to be smaller, and the particle size distribution is narrower. The grain size of the $NiTiO_3$ samples is around 1-11 μm. The average grain size is about (4.1 ± 1.9) μm. However, the grain size of the Zn-doped $NiTiO_3$ samples exhibits smaller with average grain size of (3.8 ± 1.2) μm with 10 mol.% Zn dopant concentration.

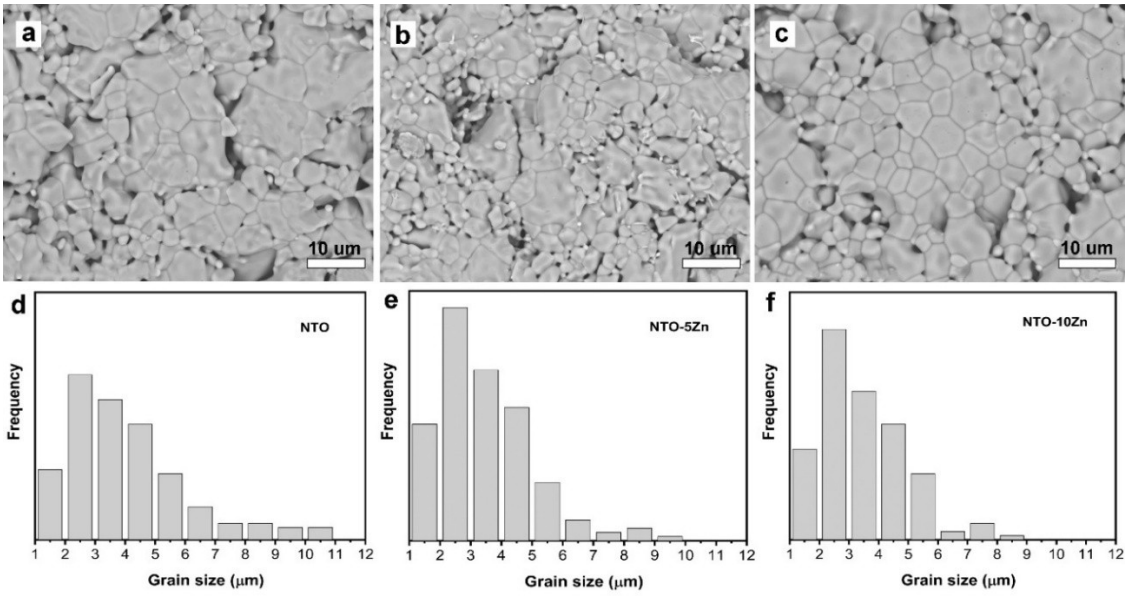

Figure 3. SEM images of (a) $NiTiO_3$, (b) 5% Zn, and (c) 10% Zn doped $NiTiO_3$ pellet surface sintered at 1200 °C for 5 hours and d-f) corresponding size distribution.

Additionally, the stoichiometric composition of the synthesized materials was confirmed through energy dispersive spectra (EDS) analysis, as shown in Figure 4. The analysis revealed the presence of Ni, Ti, Zn, and O elements in the sample, indicating that all required chemicals for the phase formation were present in the synthesized samples. The figure and the data of weight and atomic percentage compositions demonstrated that the elemental compositions and ratios are consistent with the expected elemental compositions.

To confirm the distribution of the synthesized phase, an EDS elemental mapping was conducted on the Zn-doped sample. Figure 5 illustrates the result of the EDS mapping for the Zn-doped $NiTiO_3$ sample. The EDS mapping shows the distribution of certain elements, which are depicted by unique colors. The maps of Ni, Ti, Zn, and O element show that all elements are evenly distributed in the scanned area. The color mapping of the Zn-doped $NiTiO_3$ sample (x =

0.05) compound provides the evidence of uniform distribution of elements within the compound.

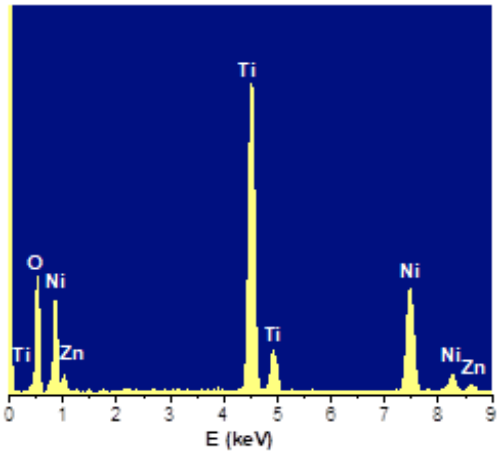

Figure 4. Energy dispersive X-ray spectroscopy of Zn doped $NiTiO_3$ sample.

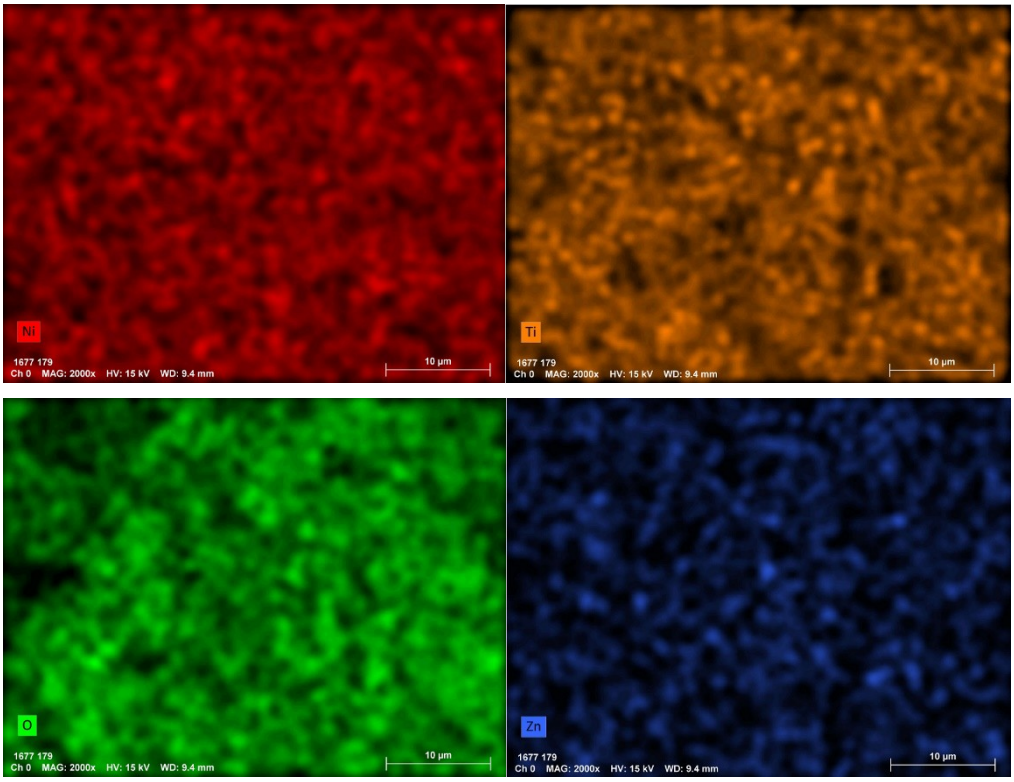

Figure 5. Energy dispersive X-ray spectroscopy mapping of the Zn-doped $NiTiO_3$ sample.

3.4. Electrical analysis

The process of electrical conduction through dielectric materials is initiated by the infusion of thermal energy. This process entails the organized migration of charged particles that are loosely bound, and the type of charge carriers involved significantly impacts the conductance.

For ceramics, the direct current (dc) conductivity can be mathematically described by an Arrhenius equation, which establishes a relationship between the conductivity at a specific temperature, the pre-exponential factor, Boltzmann's constant, and the activation energy [30].

$$\sigma_{dc} = \sigma_o \exp\left(-\frac{E_a}{k_B T}\right) \quad (2)$$

where σ_{dc} is the conductivity at temperature T, σ_0 is called the pre-exponential factor, k_B is Boltzmann's constant and E_a is the activation energy. The relationship between $\ln(\sigma_{dc})$ and the inverse of temperature (1000/T) is shown in Figure 6. This result shows that the conduction process is thermally activated, and becomes more mobile at high temperatures. The relationship between conductivity and temperature as well as doping concentration can be observed from the obtained results. It is evident that both temperature and doping concentration exert influence on the conductivity. With higher temperatures, the conductivity demonstrates a gradual rise. Similarly, an increase in Zn doping concentration also correlates with an increase in conductivity. These findings reveal that the introduction of Zn into the $NiTiO_3$ crystal results in enhancing conductivity of the material.

The activation energy depended on the Zn doping concentration, and it decreased with increasing of Zn amount. The activation energy of pure $NiTiO_3$ was 1.22 eV, but upon introducing Zn dopants into the crystal, the activation energy decreased to 1.18 eV and 0.9 eV for 5 % and 10 % Zn doping, respectively which demonstrates that a small amount of energy is enough to activate the charge carriers. With an increase in Zn doping concentration, the conductivity of $NiTiO_3$ was observed to increase. This enhanced conductivity is attributed to the Zn dopant, which entered the $NiTiO_3$ lattice and caused in the conductivity. In ferroelectric materials, the sintering process at higher temperatures often leads to a loss of oxygen and creation of vacancies, which act as mobile charge carriers. The presence of Zn dopants can increase the number of oxygen vacancies, which can further increase with an increase in doping concentration, leading to the formation of defects. The oxygen vacancies are responsible for the electrical conductivity of the ceramic samples, and during thermal agitation, they move in the lattice.

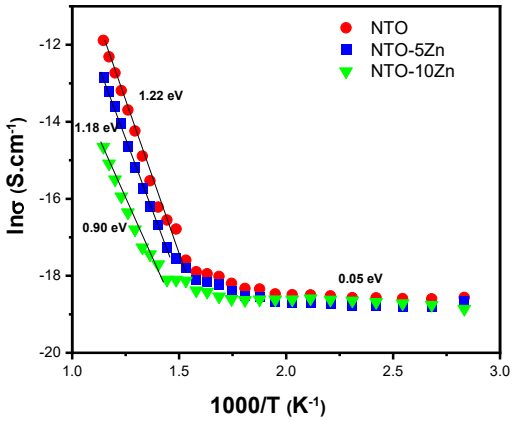

Figure 6. Arrhenius plot of DC conductivity for the $NiTiO_3$ and Zn-doped $NiTiO_3$ sample.

Figure 7 shows the variation of ac conductivity in a broad range of frequency (1 kHz - 1 MHz) at different measured temperatures. In general, the conductivity of a ceramics consists of two parts, a frequency independent dc conductivity part and a highly dispersive ac conductivity

part and this type of phenomenon can be explained by Jonscher's power law [31], given by the equation

$$\sigma(\omega) = \sigma_{dc} + A\omega^n \tag{3}$$

where n is the frequency exponent that infers the degree of interactions between the mobile ions and the lattices, σ_{dc} and A are thermally activated quantities. The ac-conductivity curves in the lower frequency region (1 kHz - 100 kHz) slightly depended on the frequency and strongly depended at the higher frequency. The doped sample, the strong dependance was occured in larger frequency region. The n value in this material depended on temperature, type of doping element and concentration of dopant. With pure $NiTiO_3$ sample, the conductance increased fast when the frequency grew up to the range from 100 kHz to 10 MHz, which demonstrates the dominant contribution of grains to the conduction compared to the contribution of grain boundaries. The conductance of $NiTiO_3$ is almost no change at frequency in range of 1 kHz – 100 kHz. With increasing the Zn dopant into $NiTiO_3$ lattice, the ac conductances are higher in comparison with that of the pure $NiTiO_3$ in all frequency range. Zn dopant can cause creating more oxygen vacancies, which leads to the formation of defects. This reason can result in dominating the contribution of grain boundaries in comparison with grain. The increment in the conductivity value of the material with growing temperature and frequency suggests an occurrence of negative temperature coefficient of resistance phenomenon.

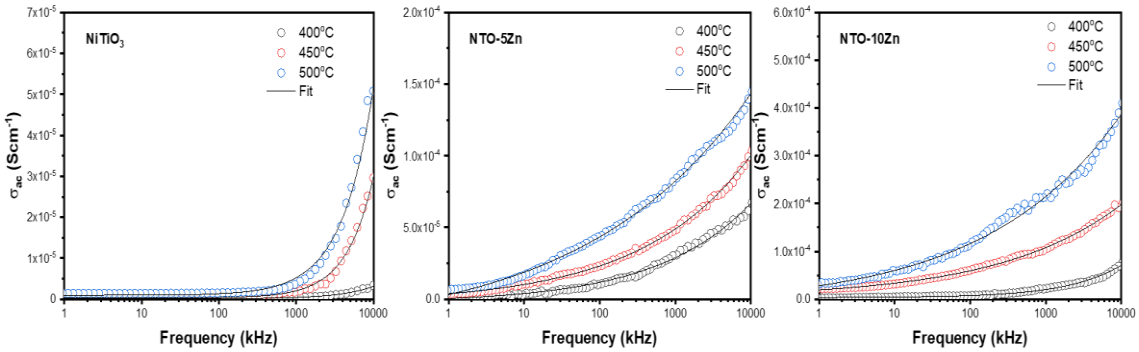

Figure 7. Frequency dependence of ac-conductivity of $NiTiO_3$ and Zn doped $NiTiO_3$.

3.5. Ferroelectric properties analysis

Figure 8 presents the results of the polarization-electric field hysteresis loops for Zn-doped $NiTiO_3$ at different applied electric fields. The P–E hysteresis loops exhibit nonlinear polarization behavior without clear saturation, particularly in the Zn-doped samples. The apparent increase in polarization with Zn content is accompanied by loop broadening and distortion, indicating significant contributions from defect-mediated conduction and space-charge polarization rather than intrinsic ferroelectric domain switching. The hysteresis loops of $NiTiO_3$ have a saturation polarization of 0.07 $\mu C/cm^2$ at an electric field of 10 kV/cm and a coercive field of 3.37 kV/cm. The addition of Zn dopant results in an increase of polarization values, and the extent of increase is directly proportional to the concentration of Zn doping. Overall, the results indicate that the introduction of Zn into $NiTiO_3$ enhances its ferroelectric properties.

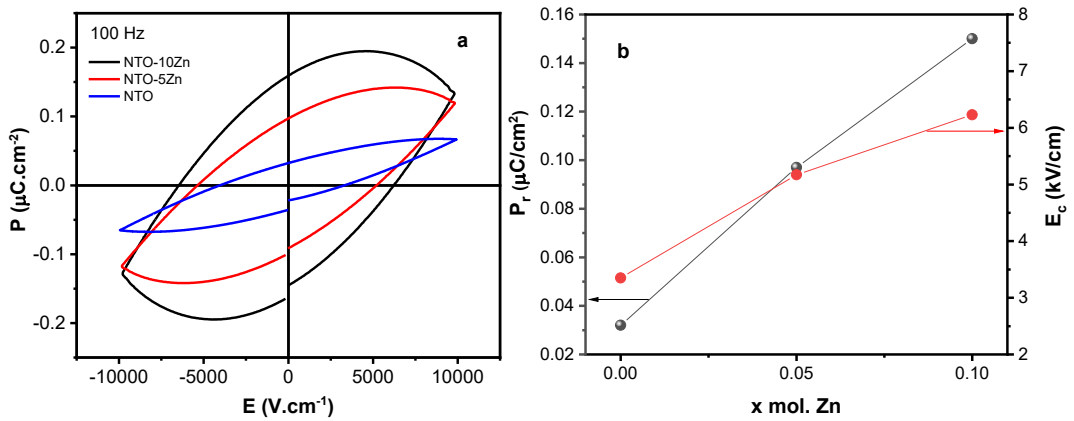

Figure 8. (a) *P-E* hysteresis loops measured on sintered pellets of Zn doped $NiTiO_3$ at different polarizing electric fields and (b) dependence of P_r and E_c on Zn doping concentration.

The incoporation of Zn into the $NiTiO_3$ lattice can lead to lattice distortion. In general, the introduction of dopants like Zn into a crystal lattice can cause local disruptions in the regular arrangement of atoms, leading to lattice distortion. This distortion can arise due to differences in atomic size, electronic interactions, and changes in the overall crystal structure. Regarding the P-E relationship, it refers to the relationship between the polarization (P) and the applied electric field (E) in a material. The ferroelectric properties of $NiTiO_3$ ceramics with different Zn doping concentrations are presented in Table 2. The presence of lattice distortion can influence this relationship. In some cases, lattice distortions can enhance the P-E response, resulting in an increase in the polarization under an applied electric field. However, in the case of heavy doping of Zn, where the dopant concentration exceeds 0.1, we observed an increase in leakage current and a degradation of the ferroelectric properties. This could be attributed to the formation of defects such as vacancies, which act as charge carriers in the crystal. The presence of these defects increases the concentration of charge carriers, thereby enhancing the material's conductivity and leakage current in heavily doped material.

Table 2. Ferroelectric properties of the $NiTiO_3$ ceramics with the different Zn doping concentration.

x	P_{max} (μC/cm^2)	P_r (μC/cm^2)	E_c (kV/cm)
0	0.072	0.032	3.35
0.05	0.14	0.097	5.17
0.10	0.19	0.15	6.23

Zn doping in $NiTiO_3$ plays a significant role in modifying both the electrical transport and polarization response of the material. Although Zn^{2+} substitutes isovalently for Ni^{2+}, its larger ionic radius induces local lattice distortion, which affects defect-assisted charge transport, as reflected by the increased electrical conductivity and reduced activation energy observed in impedance measurements. These defect-related charge carriers enhance space-charge and interfacial polarization contributions, leading to higher apparent polarization values and broadened P–E hysteresis loops in Zn-doped samples. However, the increased conductivity and delayed charge relaxation at high electric fields also result in polarization instability and loop distortion, indicating that the polarization response is dominated by non-ideal, defect-mediated mechanisms rather than intrinsic ferroelectric domain switching. Consequently, Zn doping

modifies the electrical and dielectric behavior of $NiTiO_3$ but does not lead to a clear enhancement of intrinsic ferroelectricity.

4. CONCLUSIONS

In conclusion, $Ni_{1-x}Zn_xTiO_3$ with x = 0, 0.05, and 0.10 ceramics were successfully synthesized via the sol-gel method. The effects of Zn substitutions on microstructure, conductivity and ferroelectric properties were investigated. The results show that all synthesized doped $NiTiO_3$ samples crystallized into the single ilmenite rhombohedral phase. An increase of lattice parameters values is observed with Zn addition. The Zn substitution for Ni in $NiTiO_3$ lattice resulted in increasing of conductivity. P–E measurements reveal nonlinear hysteretic polarization behavior in both undoped and Zn-doped $NiTiO_3$ ceramics. Zn substitution increases apparent polarization and electrical conductivity but also introduces stronger non-ideal effects. These results indicate that Zn doping modifies the electrical and dielectric response of $NiTiO_3$ through defect-assisted polarization mechanisms rather than enhancing intrinsic ferroelectricity. Doping of Zn resulted in increasing of conductivity and degradation of the ferroelectric properties of $NiTiO_3$. Our work is a step further to understand the role of interaction in A-site in nanocrystal ilmenite structure for electronic device application.

Acknowledgements. This research is funded by Vietnam National Foundation for Science and Technology Development (NAFOSTED) under grant number 103.02-2020.27.

CRediT authorship contribution statement. Bui Phi Long: Materials synthesis and measurement impedance spectroscopy. Nguyen Hoang Tuan: structural analysis. Pham Phi Hung: Methodology, Investigation. Nguyen Tuyet Nga: Electrical analysis. Pham Van Thang: Structural measurement and analysis. Duong Van Thiet: Electrical analysis. Luong Huu Bac: Writing, Formal analysis, Supervision.

Declaration of competing interest. The authors declare that they have no known competing financial interests or personal relationships that could have appeared to influence the work reported in this paper.

REFERENCES

1. Jing P., Lan W., Su Q., Yu M., Xie E. - Visible-Light Photocatalytic Activity of Novel $NiTiO_3$ Nanowires with Rosary-Like Shape. Sci. Adv. Mater., **6**(3) (2014) 434-440. https://doi.org/10.1166/sam.2014.1735.
2. Phi Long B., Van Thiet D., Phi Hung P., Hoang Tuan N., Huu Bac L. - Green synthesis of $NiTiO_3$ nanoparticles and sonocatalytic degradation of Rhodamine B textile dye in water. Mater. Lett., **356** (2024) 135581. https://doi.org/10.1016/j.matlet.2023.135581.
3. Wang Z., Wang Z., Yang W., Peng R., Lu Y. - Carbon-tolerant solid oxide fuel cells using $NiTiO_3$ as an anode internal reforming layer. J. Power Sources, **255** (2014) 404-409. https://doi.org/10.1016/j.jpowsour.2014.01.014.
4. More M. A., Shinde S. D., Naik N., Ezema F. I., Ahemad H. I., Jain G. H., Patil D. Y., Patil S. B., Kim J. M., Bulakhe R. N., Patil G. E. - Enhanced Physico-Chemical and Electrical Characteristics of Hydrothermally Synthesized $NiTiO_3$ via Tungsten Doping for Gas Sensing Applications. Small, **21**(42) (2025) e2505793. https://doi.org/10.1002/smll.202505793.
5. Jaye K., Moureen C., Harada J. K., Balhorn L., Hazi J., Kemei M. C., Seshadri R. - Magnetodielectric coupling in the ilmenites $MTiO_3$ (M = Co, Ni). Phys. Rev. B, **93** (2016) 104404.
6. Moghtada A., Shahrouzianfar A., Ashiri R. - Facile synthesis of $NiTiO_3$ yellow nano-pigments with enhanced solar radiation reflection efficiency by an innovative one-step method at low temperature. Dyes Pigm., **139** (2017) 388-396. https://doi.org/10.1016/j.dyepig.2016.12.044.

7. Lu C., Naresh N., Kumar P. S., Som S. - Microwave-assisted solvothermal synthesis and electrochemical characterizations of ternary perovskite $NiTiO_3$ anode materials for lithium-ion batteries. Ceram. Int., **45**(15) (2019) 19517-19521. https://doi.org/10.1016/j.ceramint.2019.06.057.
8. Shu X., He J., Chen D. - Visible-Light-Induced Photocatalyst Based on Nickel Titanate Nanoparticles. Ind. Eng. Chem. Res., **47**(14) (2008) 4750-4753. https://doi.org/10.1021/ie071619d.
9. Sadjadi M. S., Mozaffari M., Enhessari M., Zare K. - Effects of $NiTiO_3$ nanoparticles supported by mesoporous MCM-41 on photoreduction of methylene blue under UV and visible light irradiation. Superlattices Microstruct., **47**(6) (2010) 685-694. https://doi.org/10.1016/j.spmi.2010.02.007.
10. El-Maghrabi H. H., Nada A. A., Diab K. R., Youssef A. M., Hamdy A., Roualdes S., Abd El-Wahab S. - Facile fabrication of $NiTiO_3$/graphene nanocomposites for photocatalytic hydrogen generation. J. Photochem. Photobiol. A, **365** (2018) 86-93. https://doi.org/10.1016/j.jphotochem.2018.07.040.
11. Khoa V. D., Bac L. H. - Synthesis of $NiTiO_3/TiO_2$ Composite Nanoparticles by a Green Approach: Application as Sonocatalyst for Dye Degradation. J. Electron. Mater., **54**(10) (2025) 8965-8978. https://doi.org/10.1007/s11664-025-12291-x.
12. Yuvaraj S., Nithya V. D., Fathima K. S., Sanjeeviraja C., Selvan G. K., Arumugam S., Selvan R. K. - Investigations on the temperature dependent electrical and magnetic properties of $NiTiO_3$ by molten salt synthesis. Mater. Res. Bull., **48**(3) (2013) 1110-1116. https://doi.org/10.1016/j.materresbull.2012.12.001.
13. Shankar J., Kumar A. S., Kumar R. V. S. - Effect of sintering temperature on microstructure, dielectric and ferroelectric properties of $BaTiO_3$ ceramics. Ferroelectrics, **606**(1) (2023) 207-218. https://doi.org/10.1080/00150193.2023.2189837.
14. Alkathy M. S., Hezam A., Manoja K. S. D., Wang J., Cheng C., Byrappa K., Raju K. C. J. - Effect of sintering temperature on structural, electrical, and ferroelectric properties of lanthanum and sodium co-substituted barium titanate ceramics. J. Alloys Compd., **762** (2018) 49-61. https://doi.org/10.1016/j.jallcom.2018.05.138.
15. Bawa Waje S., Hashim M., Ismail I. - Effects of sintering temperature on grain growth and the complex permeability of $Co_{0.2}Ni_{0.3}Zn_{0.5}Fe_2O_4$ material prepared using mechanically alloyed nanoparticles. J. Magn. Magn. Mater., **323**(11) (2011) 1433-1439. https://doi.org/10.1016/j.jmmm.2010.12.032.
16. Chawla A., Singh A., Babu P. D., Singh M. - Analysis of phase segregation using rietveld refinement in and magnetic properties of Mn doped BCT solid solutions. Physica B, **593** (2020) 412299. https://doi.org/10.1016/j.physb.2020.412299.
17. Bac L. H., Phuong N. T., Kim Thoa D. T., Tuan N. H., Dung D. D., Diem Ngoc T. V., Hung P. P. - Structural, Ferroelectric and Magnetic Properties of $NiTiO_3$-$CoTiO_3$ Solid Solutions Synthesized by Sol-Gel Method. Int. J. Nanosci., **22**(02) (2023) 1-9. https://doi.org/10.1142/S0219581X23500102.
18. Tasneem M., Kamakshi K. - Dysprosium doping induced effects on structural, dielectric, energy storage density, and electro-caloric response of lead-free ferroelectric barium titanate ceramics. J. Mater. Sci., **59**(4) (2024) 1472-1485. https://doi.org/10.1007/s10853-023-09264-y.
19. Pham T., Kang S. G., Shin E. W. - Optical and structural properties of Mo-doped $NiTiO_3$ materials synthesized via modified Pechini methods. Appl. Surf. Sci., **411** (2017) 18-26. https://doi.org/10.1016/j.apsusc.2017.03.123.
20. Fujioka Y., Frantti J., Puretzky A., King G. - Raman Study of the Structural Distortion in the $Ni_{1-x}Co_xTiO_3$ Solid Solution. Inorg. Chem., **55**(18) (2016) 9436-9444. https://doi.org/10.1021/acs.inorgchem.6b01693.
21. Bharathi K., Chandra Babu Naidu K., Veena E., Chandrasekhar M., Baba Basha D., Siva Sankara Reddy L. - $Al_xNi_{1-x}TiO_{3+\delta}$ (x = 0.2-0.8) nanomaterials for dielectric absorber applications. J. Mater. Sci.: Mater. Electron., **36**(24) (2025) 1522. https://doi.org/10.1007/s10854-025-15598-x.
22. Jiang K., Jung H., Pham T. T., Dao D. Q., Nguyen T. K. A., Yu H., Men Y., Shin E. W. - Modification of $NiTiO_3$ visible light-driven photocatalysts by Nb doping and NbOx heterojunction: Oxygen vacancy in the Nb-doped $NiTiO_3$ structure. J. Alloys Compd., **861** (2021) 158636. https://doi.org/10.1016/j.jallcom.2021.158636.
23. Lenin N., Karthik A., Sridharpanday M., Selvam M., Srither S. R., Arunmetha S., Paramasivam P., Rajendran V. - Electrical and magnetic behavior of iron doped nickel titanate ($Fe^{3+}/NiTiO_3$)

magnetic nanoparticles. J. Magn. Magn. Mater., **397** (2016) 281-286. https://doi.org/10.1016/j.jmmm.2015.08.115.
24. Shannon R. D. - Revised Effective Ionic Radii and Systematic Studies of Interatomic Distances in Halides and Chalcogenides. Acta Crystallogr. A, **32**(5) (1976) 751-767. https://doi.org/10.1107/S0567739476001551.
25. Liu X., Hong R., Tian C. - Tolerance factor and the stability discussion of ABO_3-type ilmenite. J. Mater. Sci.: Mater. Electron., **20**(4) (2009) 323-327. https://doi.org/10.1007/s10854-008-9728-8.
26. Baraton M. I., Busca G., Prieto M. C., Ricchiardi G., Escribano V. S. - On the Vibrational Spectra and Structure of $FeCrO_3$ and of the Ilmenite-Type Compounds $CoTiO_3$ and NiTiO3. J. Solid State Chem., **112**(1) (1994) 9-14. https://doi.org/10.1006/jssc.1994.1256.
27. Ruiz Preciado M. A., Kassiba A., Morales-Acevedo A., Makowska-Janusik M. - Vibrational and electronic peculiarities of $NiTiO_3$ nanostructures inferred from first principle calculations. RSC Adv., **5**(23) (2015) 17396-17404. https://doi.org/10.1039/C4RA16400H.
28. Vijayalakshmi R., Rajendran V. - Effect of reaction temperature on size and optical properties of $NiTiO_3$ nanoparticles. E-J. Chem., **9**(1) (2012) 282-288. https://doi.org/10.1155/2012/607289.
29. Lopes K. P., Cavalcante L. S., Simoes A. Z., Varela J. A., Longo E., Leite E. R. - $NiTiO_3$ powders obtained by polymeric precursor method: Synthesis and characterization. J. Alloys Compd., **468**(1-2) (2009) 327-332. https://doi.org/10.1016/j.jallcom.2007.12.085.
30. Pu Y., Dong Z., Zhang P., Wu Y., Zhao J., Luo Y. - Dielectric, complex impedance and electrical conductivity studies of the multiferroic $Sr_2FeSi_2O_7$-crystallized glass-ceramics. J. Alloys Compd., **672** (2016) 64-71. https://doi.org/10.1016/j.jallcom.2016.02.137.
31. Jonscher A. K. - The "universal" dielectric response. Nature, **267**(5613) (1977) 673-679. https://doi.org/10.1038/267673a0.